Voltage Controlled Energy Efficient Domain Wall Synapses with Stochastic Distribution of Quantized Weights in the Presence of Thermal Noise and Edge Roughness

Walid Al Misba, Tahmid Kaisar, Dhritiman Bhattacharya, Member, IEEE, and Jayasimha Atulasimha, Senior Member, IEEE

Abstract— We propose energy efficient voltage induced strain control of domain wall (DW) in a perpendicularly magnetized nanoscale racetrack on a piezoelectric substrate that can implement a multi-state synapse to be utilized in neuromorphic computing platforms. Here strain generated in the piezoelectric is, mechanically transferred to the racetrack and modulates the Perpendicular Magnetic Anisotropy (PMA) in a system that has significant interfacial Dzyaloshinskii-Moriya interaction (DMI). When different voltages are applied (i.e. different strains are generated) in conjunction with SOT due to a fixed current flowing in the heavy metal layer for a fixed time, DWs are translated to different distances and implement different synaptic weights. We have shown using micromagnetic simulations that 5-state and 3-state synapses can be implemented in a racetrack that is modeled with the inclusion of natural edge roughness and room temperature thermal noise. These simulations show interesting dynamics of DWs with roughness induced pining sites both at the beginning and end of the SOT current pulse for different PMA modulation. Thus, notches need not be fabricated to implement multi-state nonvolatile synapses. Such a strain-controlled synapse has an energy consumption of ~ 1 fJ and could thus be very attractive to implement energy-efficient quantized neural networks, which has been shown recently to achieve near equivalent classification accuracy to the full-precision neural networks.

Index Terms—Neuromorphic computing, Synapse, Domain wall, MTJ, Edge roughness, Spin orbit torque, Magneto-elastic effect.

I. INTRODUCTION

Neuromorphic computing outperforms traditional von-Neumann type processors in data-intensive

Submitted on May 17, 2021. W.A.M., T.K, D.B. and J.A. are supported by National Science Foundation (NSF) Grants ECCS 1954589 and CCF 1815033

classification tasks. Moreover, their in-memory computing architecture can reduce energy dissipation [1] required to shuttle data back and forth between processor and memory unit in traditional computing architectures. Examples of hardware realization for neuromorphic computing include phase change random access memory (PCRAM) [2-4], resistive random-access memory (RRAM) [5,6] and spin transfer torque random-access memory (STTRAM) [7]. While the device variability is a persistent issue for all of the above-mentioned devices, recent work in fully connected artificial neural network (ANN) [8] shows equivalent accuracy to software-based training. Unfortunately, PCRAM and RRAM based devices consume energy on the order of a few pJs per synaptic weight alteration event [9]. Hence, the future IoTs and edge-devices where power is limited will necessitate alternate neuromorphic hardware that are energy efficient and enable real time programing of synaptic weights so the networks can be trained in-situ.

Recently, nanomagnet based synaptic devices has shown potential to be energy efficient compared to PCRAM and RRAM [9, 10, 11]. Among nanomagnet based neuromorphic devices, domain wall (DW) based magnetic tunnel junctions (MTJs) are one of the most promising. To implement these devices, domain walls (DWs) are translated to different positions by externally applied magnetic field [12], an electric current that causes spin-orbit torque (SOT) [13-15], spin transfer torque (STT) [16-18] or a strain gradient [19-20]. Strain control of magnetization consumes ultra-low energy [21-27]. Hence, manipulation of DWs with strain can be utilized to implement energy efficient neuromorphic devices. Recently, strainmediated control of DW has been reported [28, 29]. Strain gradient in conjunction with SOT or STT [10]

W. A. Misba, T. Kaisar, and D. Bhattacharya are with the Department of Mechanical and Nuclear Engineering, Virginia Commonwealth University, Richmond, VA 23284 USA (e-mail: misbawa@vcu.edu, kaisart@ufl.edu and dhritiman.bhattacharya@georgetown.edu)

J. Atulasimha is with the Department of Mechanical and Nuclear Engineering and the Department of Electrical and Computer Engineering, Virginia Commonwealth University, Richmond, VA23284 USA (e-mail: jatulasimha@vcu.edu)

has also been proposed to control DW position to implement energy efficient synaptic devices that can be programmed in real time.

In this work, we propose to utilize SOT to translate the DW in a realistic nanoscale racetrack modeled with edge roughness and thermal noise where the DW position is controlled by modulating the perpendicular magnetic anisotropy (PMA) of the racetrack with the application of stress. Here, deterministic control of DW to realize different synaptic values is hard to achieve when different stress values are generated by applying voltage pulse of different amplitudes to the electrodes patterned on top of a piezoelectric. This is because, equilibrium DW positions are often stochastic in nature and with the presence of defects [30], local imperfections [31] and thermal noise [32] it could be very difficult to achieve deterministic control. Nevertheless, the DW can be arrested by providing trap sites such as curved shape [33] and notch or protrusion [34], which can act as a potential well or barrier. Moreover, edge roughness [35-36] can introduce pinning sites for DW motion. In this paper, we use edge roughness and obtain the statistical distribution of DW position from micromagnetic simulations which shows that the mean positions are different for different stress induced change of PMA for a fixed current induced SOT of a fixed "clock" time. Although the number of states (different DW positions) attained are limited and there are overlaps between the states, such a DW based racetrack as synapse is particularly attractive to implement quantized deep neural networks (DNN) [37-39] as these networks have been shown to reach accuracy very close to the infinite states network. The overlap between states can be addressed during the training stage of a learning network. Moreover, the stochastic variation of a state can be useful in generating stochastic weights for training the network which can work as DNN regularizer to reduce overfitting of training [40]. Studies have shown training with stochastically determined weights rather than deterministic ones can potentially increase the classification accuracies for some data sets [37].

II. METHOD

The proposed device structure is illustrated in Fig. 1(a). The stack consists of a heavy metal layer and a magnetic tunnel junction (MTJ) containing the nanoscale racetrack as free layer, along with the tunnel barrier and the hard layer. Such a stack is patterned on top of a piezoelectric substrate. We consider Pt/CoFe (soft or free racetrack layer)/MgO/CoFe (hard or fixed layer) as our stack materials where the heavy metal layer Pt will create perpendicular anisotropy and

strong DMI at Pt/CoFe interface, which is known to favor the chiral Neel DWs [41]. We propose to arrest the DWs at different positions in the free layer of the MTJ, which will modify the resistance value of the MTJ stack. Thus, different synaptic weights, which define the strength between the neurons can be determined from the DW positions. Different layers of a DNN can be implemented by arranging the DW devices in the crossbar as shown in Fig. 1(c), where the DW devices provide the programmable conductances which are equivalent to the DNN weights.

To arrest the DW at various positions we apply different amplitude stress in combination to a fixed amplitude and fixed duration SOT pulse. When a voltage is applied between the electrodes on top and bottom of the piezo-substrate as shown in Fig. 1(b), mechanical strain is generated. This strain is then transferred to the racetrack and consequently modulates the perpendicular anisotropy due to magnetoelastic interaction. In combination with stress, we apply a current pulse in the adjacent heavy metal Pt layer to exert SOT shown by red arrow in Fig. 1(b), which moves the DW through the nanowire racetrack to the other end of the nanowire. If we reverse the direction of current in the heavy metal layer, it will reverse the direction of DW motion and reset it to the other end.

We have considered edge roughness that is present naturally in a nanoscale racetrack due to lithographic imperfection and pattern transfer process. Authors report [42] ~ 2nm rms edge roughness for 25 nm wide racetrack when they use a combination of electron beam lithography (EBL) and ion beam etching. Authors [36] also report ~ 2nm rms edge roughness for 80 nm wide racetrack using the same method. However, studies have shown higher rms edge roughness for low voltage EBL for racetrack of width 50 nm or higher [42]. For our simulation we have assumed Gaussian distribution for the edge roughness with a rms value of ~ 3nm considering the effect of high electron jitter from mean position for low voltage EBL. In addition to the local structure variation, microstructure in the racetrack such as grain boundary, defects can provide pinning sites and introduce stochasticity in the devices. We did not consider these in our simulation for sake of simplicity. The simulated racetracks have a length of 500 nm, maximum width of 50 nm and thickness of 1 nm. The magnetization dynamics in the presence of Spin Orbit Torque (SOT) is simulated in MUMAX3 [43] using the Landau-Lifshitz-Gilbert-Slonczewski equation:

$$(1 + \alpha^2) \frac{d\vec{m}}{dt} = -\gamma \vec{m} \times \vec{H}_{eff} - \alpha \gamma \left(\vec{m} \times (\vec{m} \times \vec{H}_{eff}) \right) - \beta \gamma (\varepsilon - \alpha \varepsilon') (\vec{m} \times (\vec{m}_P \times \vec{m}))$$

$$+ \beta \gamma (\varepsilon' - \alpha \varepsilon) (\vec{m} \times \vec{m}_P)$$
(1)

$$\beta = \frac{\hbar J\theta}{\mu_0 e dM_s},$$

$$\epsilon = \frac{P\Lambda^2}{(\Lambda^2 + 1) + (\Lambda^2 - 1)(\vec{m} \cdot \vec{m}_p)}$$
(2)

We consider secondary spin torque parameter to be $\varepsilon' = \alpha \varepsilon$ and neglect the field like torque. Here, $\vec{m}_P =$ $\vec{J}_x \times \vec{z}$ where *J* is the value of current flowing through the heavy metal layer and \vec{J}_x is the unit vector defining the direction of current flow and \vec{z} is the direction of inversion asymmetry. Here, θ is the spin Hall angle which is 0.1 for Pt [44], γ is the gyromagnetic ratio, \vec{m} is the unit magnetization vector, M_s is the saturation magnetization, \hbar is the reduced Planck constant, μ_0 is the permeability of free space, e is the electron charge and d is the thickness of the nanowire. To equate the Slonczewski toque with Spin orbit torque we assume spin polarization to be P = 1 and Slonczewski parameter to be $\Lambda=1$. Here the effective field, \vec{H}_{eff} accounts for the contributions from demagnetization, Heisenberg exchange PMA. interaction. Dzyaloshinskii-Moriya interaction (DMI), stress induced anisotropy and thermal noise. \vec{H}_{eff} can be expressed as follows:

$$\vec{H}_{eff} = \vec{H}_{anis} + \vec{H}_{demag} + \vec{H}_{stress} + \vec{H}_{exch} + \vec{H}_{thermal}$$
(3)

The racetracks are discretized into 2 nm \times 2 nm \times 1 nm cells which are well within the ferromagnetic exchange length of $\sqrt{\frac{2A_{ex}}{\mu_0 \, M_s^2}} = 5.66$ nm. We note that curved edges are difficult to approximate with finite difference method as it depends on stair case approximation. As a result, the demagnetization tensor is not computed properly [45-47]. However, we find similar trend in our result when we decrease the cell size.

PMA induced effective field can be expressed as, \vec{H}_{anis} :

$$\vec{H}_{anis} = \frac{2K_u}{\mu_0 M_c} (\vec{u}.\vec{m}) \vec{u} \tag{4}$$

Where K_u is the first order anisotropy constant and \vec{u} represents the uniaxial anisotropy direction (i.e. perpendicular to plane).

If the electrodes patterned on top of the piezoelectric substrate have dimensions similar to the piezoelectric thickness and separated by one or two times the piezoelectric thickness, maximum stress is generated [48]. In such a scenario, when a positive (negative) voltage is applied in the top electrode pair, the area underneath the electrode become stretched (compressed) in the out of plane direction and compressed (stretched) in the in-plane direction. Compression (tension) in the in-plane direction underneath the electrode surface creates tension (compression) in the nanoscale racetrack patterned in between the top electrodes due to strain-displacement compatibility. We assumed our electrodes to be rectangular with width b=piezoelectric thickness and length L=racetrack length. This is similar to having (L/b) number of square electrodes of (b×b) dimensions and therefore one can assume this electrode configuration will produce similar amount of stress as mentioned in Ref [46]. Fig. 1(b) shows the strain formation in the nanoscale racetrack in such a scenario. Stress produced in the in-plane direction of the racetrack induces anisotropy field due to the magneto-elastic effect in the same direction and modulates the PMA or the anisotropy constant K_u . The effect of the stress is modeled by the modulating K_{ν} in the micromagnetic simulation. For simplicity, we did not consider the strain that can be produced in the inplane direction of the racetrack which is orthogonal to that shown in the Fig. 1(b).

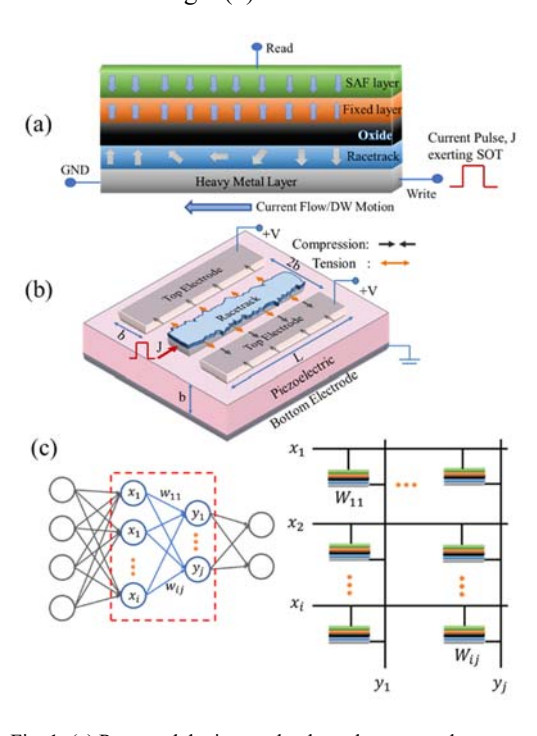


Fig. 1: (a) Proposed device stack where the nanoscale racetrack act as the magnetic free layer of the MTJ. DW in the racetrack moves when a current is applied to the heavy metal layer underneath

the racetrack (b) Stress generation mechanism in rough edge racetrack when a voltage is applied across the piezoelectric. (c) Implementation of layers of DNN with DW based synaptic devices. The devices are arranged in crossbar to provide programmable conductance equivalent to the DNN weights.

The effective field due to the interfacial Dzyaloshinskii-Moriya interaction is expressed as follows [43]:

$$\vec{H}_{DM} = \frac{2D}{\mu_0 M_s} \left(\frac{\partial m_z}{\partial x}, \frac{\partial m_z}{\partial y}, -\frac{\partial m_x}{\partial x} - \frac{\partial m_y}{\partial y} \right)$$
(5)

Here, D is the DMI constant and m_x , m_y and m_z are the x, y and z component of unit magnetization vector \vec{m} respectively.

Thermal noise induces a random effective field $\vec{H}_{thermal}$ [49]:

$$\vec{H}_{thermal} = \vec{\eta} \sqrt{\frac{2\alpha kT}{\mu_0 M_s \gamma \Omega \Delta}}$$
 (6)

Here, $\vec{\eta}$ is a random variable with Gaussian distribution with mean zero and unit variance and independent (uncorrelated) in each of the 3 cartesian coordinates generated at each time step, k is Boltzmann constant, Ω is the cell volume, Δ is the time step size.

The parameters for the simulation are presented at table I [50-52].

TABLE I

Parameters	Values
DMI constant (D)	$0.001 Jm^{-2}$
Gilbert damping (α)	0.015
Saturation magnetization (M_s)	$10^6 Am^{-1}$
Exchange constant (A_{ex})	$2 \times 10^{-11} Jm^{-1}$
Saturation magnetostriction (λ_s)	250 ppm
Perpendicular Magnetic	$7.5 \times 10^5 Jm^{-3}$
Anisotropy (K_u)	

The synaptic state of the proposed device could be read by the MTJ. For a read voltage applied between the read and GND terminal (as in Fig. 1(a)) the resistance is provided by the portion of the racetrack that is parallel (P) and antiparallel (AP) to the fixed layer and a small DW region where the magnetization is transverse to the fixed layer magnetization. The read current also counters a resistance from heavy metal layer however that is small compared to the tunnel magnetoresistance. If we assume the conductance of the racetrack is $G_{max,P}$ when completely in P state with

respect to the fixed layer and $G_{min,AP}$ when completely in AP state, then for any intermediate position q of the DW inside the racetrack of length L, the conductance of the synapse can be expressed as the following:

$$G(q) = G_{max,P}\left(\frac{q}{L}\right) + G_{min,AP}\left(1 - \frac{q}{L}\right) + G_{DW}$$
 (7)

III. RESULTS AND DISCUSSION

A. Effect of edge roughness on Domain Wall motion

In rough edge racetrack the racetrack width varies, so local pinning sites are created randomly along the length of the racetrack. Depending on the magnitude of the edge roughness (rms value or standard deviation) the pinning strength of the pining sites varies. Studies have shown that higher magnitude edge irregularities require higher depinning current to translate DW in the racetrack [53-55]. Thus, the magnitude of the edge roughness influences the equilibrium DW positions in the racetrack. This also determines the operating current of the DW based synaptic device.

In addition to the rms edge roughness, the pining location distribution or the relative position of the pining sites from DW start position and center of the racetrack influences the final DW position. The characteristic DW motion equation during the acceleration phase (at the time of SOT excitation) can be found by linearizing the 1-D DW equations [41,56]. The following Newton-like motion equation is obtained:

$$m^* \frac{dv}{dt} + \frac{m^*}{\tau} v = F \tag{8}$$

Where the effective DW mass can be expressed as:

$$m^* = \frac{1 + \alpha^2}{\gamma^2 \Delta} \tag{9}$$

The friction force is:

$$F_{fric} = \frac{m^*}{\tau} v = \frac{1}{\nu \Delta} \left(\alpha H_K + \frac{\pi}{2} H_{SH} \right) v \tag{10}$$

And the external force is:

$$F = H_{PIN}(q)H_K + \left(\frac{\pi}{2}\right)^2 H_{DM}H_{SH}$$
 (11)

Here, H_{DM} [41] is the DMI field, H_{SH} is the damping like spin hall effective field and H_K is the shape anisotropy field from magnetostatic origin.

$$H_{DM} = \frac{D}{\mu_0 \Delta M_S} \tag{12}$$

$$H_{SH} = \frac{\hbar J \theta}{2\mu_0 e dM_S} \tag{13}$$

Here, Δ is the DW width which can be expressed as:

$$\Delta \sim \sqrt{\frac{A_{ex}}{K_u - \frac{1}{2}\mu_0 M_s^2}} \tag{14}$$

The pinning field can be expressed as:

$$H_{PIN}(q) = -\frac{1}{2\mu_0 M_s w d} \frac{d[V_{PIN}(q)]}{dq}$$
 (15)

Where $V_{PIN}(q)$ is the local pinning potential due to the roughness induced pinning locations and w is the racetrack width, d is the racetrack thickness.

From the linearized motion equation of the DW we can see that the roughness induced pinning sites induce an attractive force towards the pining site scaled by the magnetostatic field $(H_{PIN}(q)H_K$ term in external force Eq. 11). This force is added to the SOT current induced force due to H_{SH} field. The demagnetization field, H_K is maximum at both ends of rectangular shape racetrack and starts to decrease and becomes minimum at the center of the racetrack. Similarly, the pining field, $H_{PIN}(q)$ is high (low) away from (close to) the pining site, however the range of this force is much more localized than the demagnetization force. Depending on the PMA modulation (different value of K_u), $H_{PIN}(q)$ changes, thus the competition between $H_{PIN}(q)$ and H_K changes. This competition eventually determines the relationship between the pining site distance from the DW and the corresponding kinetic energy (depinning current) to overcome that pining site.

When the SOT current pulse is withdrawn, the DW starts to decelerate and the deceleration force can be obtained by linearizing the 1-D DW equations:

$$F = -\left(H_K - \frac{\pi}{2}H_{DM}\right)H_{PIN}(q) \tag{16}$$

As $H_{PIN}(q)$ and H_K are both functions of distance, the magnitude of the deceleration force acting on the DW changes with the DW position in the racetrack for a fixed PMA. Thus, the DW position at the end of the SOT pulse also influences the equilibrium DW position.

B. Non-thermal Statistics due to Different Edge Roughness Profiles in Different Racetracks

For non-thermal simulations we have simulated the DW motion in 40 different racetracks with different edge roughness profile. The PMA of the racetracks is considered to be 7.5×10^5 J/m^3 . The PMA can be decreased or increased uniformly over the whole racetrack by applying a suitable voltage to the electrodes. The clocking SOT current is applied simultaneously with this voltage pulse. We have assumed that the DW is initialized to a pinning site located at one end of the racetrack. The SOT current translates the DW while the PMA modulation helps to drive the DW to different positions when clocked with SOT for a fixed time. This could be explained as following.

The critical depinning current density J_C of the DW is related to the anisotropy coefficient K_u of the racetrack. When K_u is higher, the potential well of a pinning site becomes deep, so it requires high depinning current, J_C to depin a DW siting in such a potential well or energy minima. On the contrary, lower K_u is associated with a shallow potential well for the same pinning site hence requires lower threshold current to depin. Fig. 2(a) presents a sketch of an example racetrack where the DW is situated at a pinning site located near the right end of the racetrack and Fig. 2(b) plots the depinning current versus the anisotropy coefficient for that DW. From Fig. 2(b) we can see that critical depinning current J_C is increased with the increase of anisotropy coefficient K_u .

The DW velocity at steady state can be expressed by the following [56,57]:

$$v = \frac{\pi}{2} \frac{\gamma \Delta H_{DM}}{\sqrt{(1 + (\frac{J_D}{J - J_C})^2)}}$$
(17)

$$J_D = \alpha J H_{DM} / H_{SH} \tag{18}$$

Empirical critical current density J_C is used to account for the pinning effect which is validated by fitting one dimensional DW model to the experimental data [56].

As seen from Fig. 2(b), the critical current density J_C is high for higher K_u . As a result, for a higher K_u , for a fixed clocking SOT current $J > J_C$, the velocity becomes small as the denominator in Eq. 17 is large compared to the case of lower K_u for which the denominator is small (low critical current density J_C) and velocity is high. In addition, when K_u increases (decreases) the DW width Δ in Eq. 14 decreases (increases) which increases (decreases) J_D in Eq. 18

and the denominator in Eq. 17, consequently the velocity decreases (increases).

The DW position for different anisotropy constant K_u is shown in Fig. 2(c) for one rough edge racetrack where the SOT current of $24 \times 10^{10} \ A/m^2$ is applied for fixed 1.2 ns. The change in velocity with the change in K_u is evident as the DW translates to different distances with the same SOT. After the withdrawal of the SOT and strain, the DW further moves at terminal velocity due to the momentum gained because of the SOT toque. The lower the anisotropy constant the higher the velocity gain and the higher the distance travelled by the DW after the withdrawal of SOT as can be seen for the case of $K_u = 7.3 \times 10^5 \ J/m^3$. Notably, the DW for $K_u = 7.0 \times 10^5 \ J/m^3$ also traveled same distance as $K_u = 7.3 \times 10^5 \ J/m^3$ as the velocity difference after SOT withdrawal is small and there is no suitable pining site in between to pin and stop the DW at a different position due to the small velocity difference.

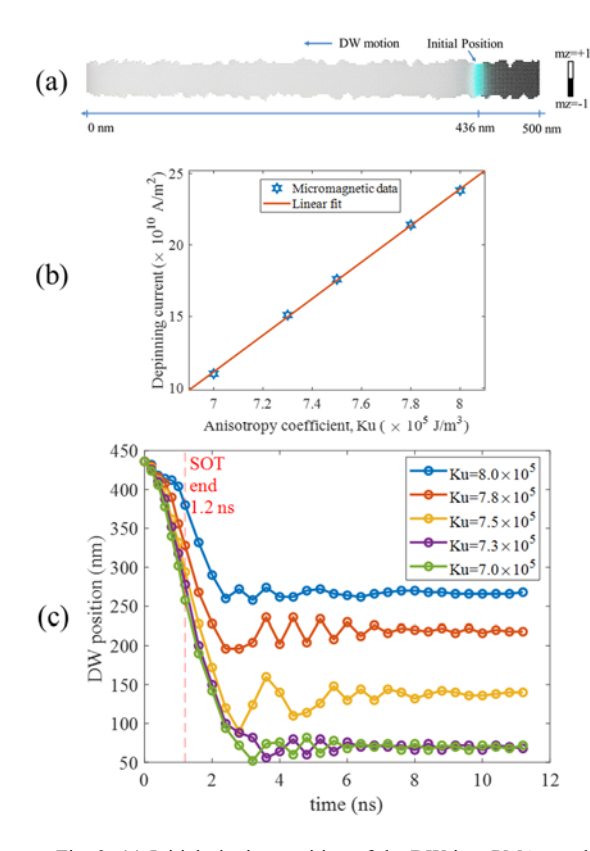


Fig. 2: (a) Initial pinning position of the DW in a PMA rough edge racetrack. (b) dependence of the DW depinning current on the anisotropy coefficient when the DW in racetrack 2(a) is in the initial pinning position. (c) DW positions with time in racetrack 2(a) for a fixed duration and amplitude current pulse exerting SOT and different stresses (different K_u). The SOT and stress are withdrawn at 1.2 ns. For different stresses respective DWs travel different distances and get pinned to different locations.

We have simulated a total of 40 racetracks of ~ 3nm rms edge roughness where we varied anisotropy constant values K_u to 8.0, 7.8, 7.5, 7.3 and 7.0 (× 10⁵) I/m^3 in each of these racetracks and applied SOT current of fixed amplitude $24 \times 10^9 A/m^2$ for 1.2 ns. Each of the DW is initialized to a pinning site located near the right end of the racetrack. After the simultaneous withdrawal of the SOT and stress we wait for 10 ns to allow sufficient time for the DW to decelerate and get pinned to a specific position. We note that, the DWs usually settle within approximately ± 4 nm of the equilibrium pinning locations after 10 ns of SOT withdrawals which is approximately 3x of the deceleration time constant calculated from 1-D DW equations. The distribution of the final DW position for the 40 racetracks is shown in Fig. 3.

In Fig. 3 for each K_u value we also overlay a gaussian distribution with identical mean and standard deviation of the data used to create the bins. Although the final position distribution does not follow Gaussian distribution, we see that the mean final positions are different for different stress (K_u) values (Fig. 3(a)-(e)). The mean DW positions shift to the left of the racetracks as we decrease the PMA. The primary source of the distribution of final DW positions for a specific K_u could be attributed to the interaction of the DWs with the roughness induced pining sites during the acceleration and deceleration phases of DW motion. During the acceleration phase the kinetic energy (or SOT current) required to overcome a pining site depends on the relative distance of the DW from the pining sites. Different racetracks offer pining sites at different locations, thus influences the equilibrium DW positions distribution. Similarly, during the deceleration phase, DW loses momentum due to damping and begins to interact strongly with the edges due to the deceleration force exerted towards the roughness induced pining sites (as seen from Eq. 16). DW-edge interaction varies among racetracks due to their different roughness profile (distribution of pining sites is different). Moreover, for different racetrack the DWs begin deceleration from different positions so the deceleration forces acted on the DWs become different. All of these factors contribute to the DWs being pinned at random positions for different racetracks. In addition to that, DWs in different racetracks are initialized from pinning sites that have different longitudinal position and geometry for different racetracks. Pinning site geometry affects the depinning current J_c vs. K_u relationship and thus different geometry can add stochasticity to the final DW position. Adding a fixed geometry notch at one end of the racetracks for DW initial location could address this stochasticity (though it cannot be addressed fully due to different stray fields for different racetracks). However, more importantly, significant stochasticity still persists (in spite of the notch to have the same initial DW starting point) due to the above-mentioned DW-edge interaction both at the beginning and end of SOT excitation.

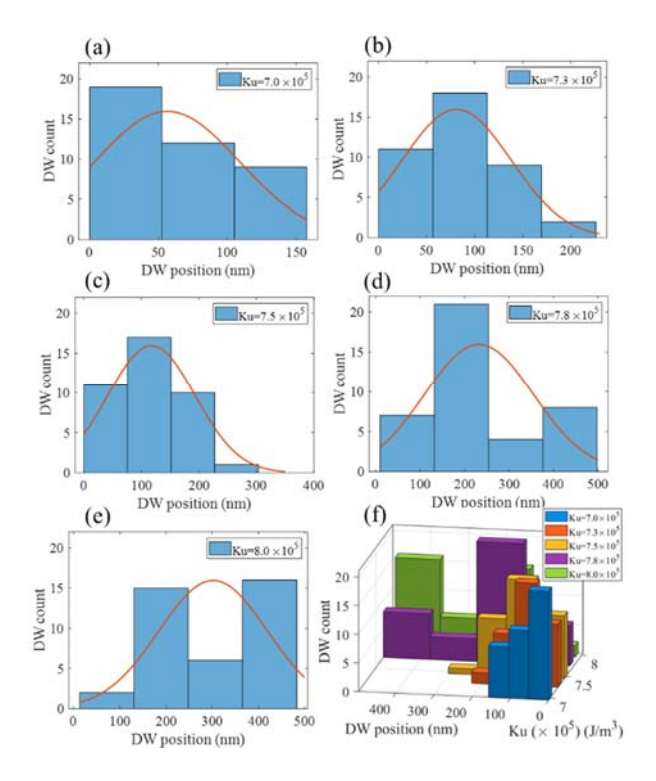


Fig. 3: (a)-(e) Equilibrium DW positions in 40 different racetracks at T=0 K for a fixed SOT and different stresses correspond to K_u values of 8.0, 7.8, 7.5, 7.3 and 7.0 (× 10^5) J/m^3 . For each figure in 3(a)-(e) a Gaussian distribution plot is overlaid having a mean and standard deviation identical to the data used to create the bins (f) 3-dimentional histogram shows combined plot of 3(a)-(e).

C. Thermal Statistics

At room temperature, the thermal perturbation can dislodge the DW. Hence, edge roughness of ~ 3 nm cannot offer similar pinning effect in thermal cases as in the non-thermal cases. As a result, the depinning current decreases in the presence of room temperature thermal noise for the same racetrack. For thermal simulation, we use a fixed clocking SOT current density of 15 \times 10¹⁰ A/m^2 which is smaller than the current density we use in non-thermal case. The SOT and stress application time are kept the same as before (1.2 ns). After the withdrawal of SOT and stress, we relax for 10 ns (as we did earlier for the non-thermal case). Unlike non-thermal cases, the DWs do not settle to a specific pinning site but oscillate around this pinning site as the thermal energy causes the DW position to fluctuate around the equilibrium position. We found that DWs usually encounter a pinning site

within 6 ns of SOT withdrawal. So, a relaxation time of 10 ns is enough for the DWs to reach an equilibrium position. We changed the anisotropy constant, K_{ν} values to 8.0, 7.8, 7.5, 7.3 and 7.0 (\times 10⁵) I/m^3 and ran the simulation for each K_u value 100 times considering limited computational resources and time. The equilibrium DW position distribution for one such racetrack of ~ 3nm rms edge roughness is shown in Fig. 4. Here, we also overlay Gaussian distribution with identical mean and standard deviation of the data used to create the bins. The bins in Fig. 4(a)-(e) are sized according to the standard deviation of the data. Although the distribution does not follow Gaussian distribution, the mean positions for different K_{ij} follow the same trend as in non-thermal case where for lower K_u values the mean DW position shifts to the left. Due to the random variation of the DW internal magnetization angle in the presence of thermal noise, upon encountering a potential barrier (or a well), the DW could overcome the barrier (or gets attracted to the well) in some cases but not in other cases. This leads to a distribution.

The settling time of 10 ns for the DW or a total write time 11.2 ns may indicate a slower device compare to SOT-MRAM based memory device where low switching time is expected. However, for hardware implementation of DNN, 11.2 ns write time is not considered too slow, as different layers in DNN are implemented with separate crossbars (as shown in Fig. 1(c)) thus can take advantage of parallel operation. Performing the weighted sum operation during the forward and backward pass of DNN consumes time (read operation), so does the activation function computation. Thus, when a crossbar implements forward pass or backward pass of one layer, the other crossbar devices can be programmed (write operation) to achieve target conductance values.

D. Determination of Synaptic State

If the number of target states are n, and the maximum and the minimum conductance of the racetrack are $G_{max,P}$ and $G_{min,AP}$, then $\sim (G_{max,P} - G_{min,AP})$ can be divided into n-1 parts to represent one state. In such a scenario, the target conductances for each of the n states can be $\sim G_{min,AP}$, $G_{min,AP} + \frac{G_{max,P} - G_{min,AP}}{n-1}$, $G_{min,AP} + 2 * \frac{G_{max,P} - G_{min,AP}}{n-1}$,, $G_{max,P}$ For any programming voltage pulse, representing by a specific PMA or Ku, the probability by which any stabilized DW provides conductance G that is within the range of target conductance G that is within the range of target conductance G that state for that programming condition. Fig. 5(a) and (b) plots the cumulative probability of DW device

conductance at T=300 K for five and three different programming conditions that implements 5- and 3state synapse. For the conductance calculation, Eq. 7 is used and the resistance area product and TMR are assumed to be $4.04 \times 10^{-12} \Omega m^2$ and 120 % [9]. The value of G_{DW} is small and neglected for calculation. In Fig. 5, the black dotted lines represent the target conductance of a state and the adjacent red dotted lines represent the state boundaries. For 5-state synapse the target conductance are chosen to be 3.22, 3.86, 4.5, 5.14 and 5.78 mS which can be achieved by modulating the PMA to 8.0, 7.8, 7.5, 7.3 and 7.0 (\times 10^5) I/m^3 respectively. For 3-state synapse the target conductance are chosen to be 3.22,4.5 and 5.78 mS. Ideally one would want 100% probability for a state for one programming condition or a specific Ku. However, in the case of stochastic DW, we get a finite probability for all the states for one programming condition. This leads to overlap of states which could degrade the ANN accuracy. These overlaps can be easily addressed by restricting the conductance of a state within the range of a target conductance (given by the adjacent red lines) by programming and then sensing or performing read-verify-write operation in a loop [58]. "Closed loop on device" [59] method can be used to perform read-verify-write operation for onchip learning and "open loop off device" [60] method can be used for off-chip learning where the target conductance values are calculated beforehand by training a precursor neural network. Comparing Fig. 5(a) and (b) we can see that the state boundary is wide for 3-state synapse, thus one state can be programmed with smaller number of attempts.

While the nanoscale racetrack could be used as a synaptic device after addressing the state overlap issue, however, the presence of device to device variation (as in Fig. 3) and intra-device variation (as in Fig. 4) are also evident. Intuitively such variation could be harmful to the functioning of the DW based synaptic device as an inference engine for classification task, as the synaptic weights obtained after software-based training cannot be programmed accurately during inference stage. However, recent studies [40] have shown that addressing the device variability during the training stage can achieve high inference accuracies that is very close to baseline accuracy (no device variability is assumed) and the accuracy is highest when the level of noise (because of the device variability) injected during the training is on the same order as the noise of the device used for the inference task.

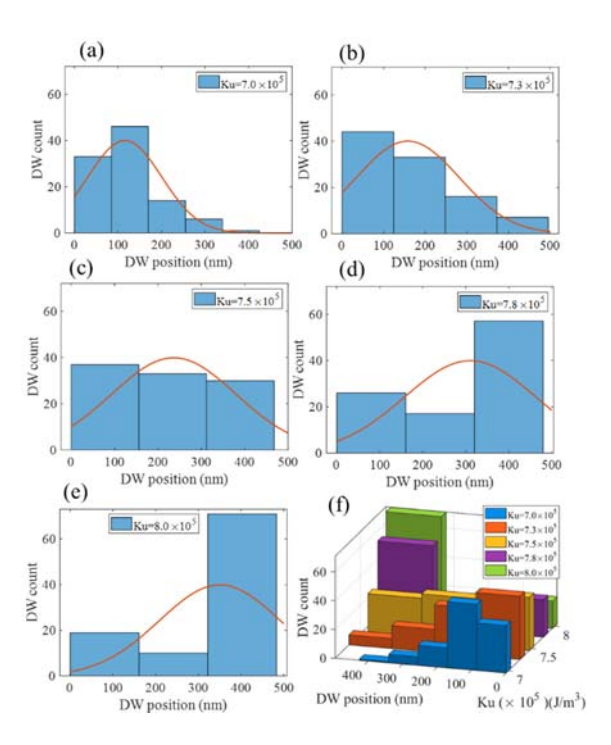


Fig. 4: (a)-(e) Equilibrium DW positions in one racetrack (\sim 3nm rms edge roughness) at T=300K for a fixed SOT and different stresses correspond to K_u values of 8.0, 7.8, 7.5, 7.3 and 7.0 (\times 10⁵) J/m^3 . For each figure in 4(a)-(e) a Gaussian distribution plot is overlaid having a mean and standard deviation identical to the data used to create the bins (f) 3-dimentional histogram shows combined plot of 4(a)-(e)

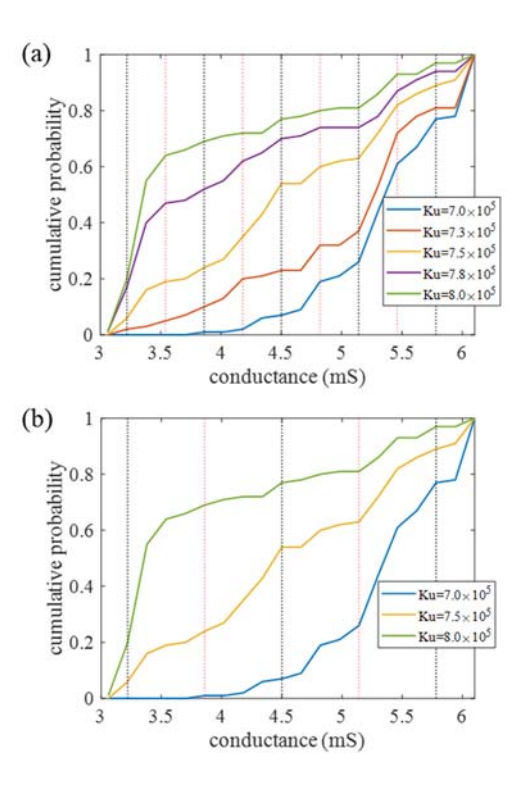


Fig. 5: (a) Cumulative probability of device conductance for 5 different programming conditions (different K_u) implementing a 5-state stochastic synapse. The black dotted lines represent the 5 target conductances for the 5-state synapse. The red dotted lines represent the boundaries of each state to ensure that no overlap happens between adjacent states. (b) Cumulative probability of device conductance for 3-state synapse. The red dotted lines represent the state boundaries. of each state. For 3-state synapse the width of state boundary is high so one state can be programmed with a smaller number of attempts.

E. Energy Dissipation

Energy dissipation in our proposed device depends on charging the piezoelectric layer as well as I^2R loss of the clocking current through the heavy metal layer. To introduce stress, we have to charge the piezoelectric layer. Energy required to charge this capacitive layer is $\frac{1}{2}CV^2$, where, V is the voltage applied and C is the capacitance of the piezoelectric layer between the metal contacts.

In our proposed device, the racetrack PMA we have considered is $K_u = 7.0 \times 10^5 J/m^3$ and the maximum change of PMA with voltage induced stress is Δ PMA=0.5 × 10⁵ J/m^3 to achieve $K_u = 7.0$ or 8.0 (× 10^5) I/m^3 . The saturation magnetostriction of CoFe is, λ_s =250 ppm. Using the above values, the maximum amount of required stress, σ is calculated to be, $\frac{\Delta PMA}{3/2\lambda_s}$ = 133 MPa. For CoFe with Young's Modulus of 200 GPa, the required strain is, $\frac{133 \, MPa}{200 \, MPa} \sim 10^{-3}$. Previous study [48] showed that 10^{-3} strain is possible in Lead Zirconate Titanate (PZT) piezoelectric with an applied electric field of $E=3MVm^{-1}$ when the electrode dimensions are in the same order of the PZT thickness. If we consider our PZT layer to be b=50 nm thick (same as top electrode or racetrack width as shown in Fig. 1(b)) then a voltage of, E*b = 0.15 V applied at the top electrode pair can generate the required strain. If the top electrode length L=500 nm (same as racetrack length 500 nm) and width b=50 nm is considered, and relative permittivity of PZT is ϵ_r =3000 then the effective capacitance is calculated to be $\frac{\epsilon_0 \epsilon_r (L^* b)}{b} \sim 13.3$ fF. This suggests a $\frac{1}{2} CV^2$ loss of ~ 0.3 fJ considering two top electrodes on both sides of the racetrack.

For our SOT clocking, we assume resistivity of Pt layer is 100Ω nm. We also assume Pt layer to be 5 nm thick, which is greater than the spin diffusion length of ~2 nm [44] and the spin hall angle to be 0.1 [44]. If a clocking current density of $24 \times 10^{10} \ A/m^2$ is applied through the Pt layer of length 500 nm, width 50 nm and thickness 5 nm for a clocking period of 1.2 ns, then the I^2R loss incurred is calculated to be ~0.86 fJ. Therefore, our proposed DW based device can

program the synapse with maximum energy dissipation of approximately 1.16 fJ.

Energy consumption to program the proposed synapse to the maximum (or minimum) conductance value is 1.16 fJ which is much less than previously reported [10,11]. Recent study has shown DW based synapse with racetrack dimension of 1000 nm x 50 nm, where each synaptic state is programmed by applying SOT current pulse for 3 ns [9]. In their device they require ~ 8.64fJ to program the synaptic conductance from one extreme to the other. While the state-of-theart phase change memory (PCM) device and the metal oxide resistive random-access memory (RRAM) device can have a smaller footprint, however, the programming energy can be as high as several pJs [9, 61] because these devices involve physical movement of ions. Moreover, the endurance cycle of the of the PCM and the RRAM devices are low compare to spintronic DW devices [62].

IV. CONCLUSION

In summary, we have proposed an energy efficient strain-controlled synapse where different synaptic weights have been achieved by applying different values of voltage induced stress in conjunction with a fixed clocking SOT current in chiral DW systems with significant DMI. While a uniform change in stressinduced anisotropy cannot move the DW that is pinned in a trap site, it can influence the potential landscape such that the DW in a low PMA racetrack moves faster than in a high PMA one, when being driven by a fixed SOT current. We have showed that five different mean equilibrium DW positions with five different voltage induced stress values is achievable in a 500 nm long and 50 nm wide racetrack with edge roughness of ~3 nm. These suggest the feasibility of a 5-state synapse A 3-state synapse can be also achieved using three different voltage induced PMA modulation. Recent progress in low precision quantized neural network to achieve near equivalent accuracy to full-precision network makes such a DW based synapse device specifically attractive as a powerful classification tool for edge devices where energy requirement is at a premium.

REFERENCES

[1] A. Pedram, S. Richardson, M. Horowitz, S. Galal, and S. Kvatinsky, "Dark Memory and Accelerator-Rich System Optimization in the Dark Silicon Era", IEEE Design & Test, vol. 34, no. 2, pp. 39-50, Apr. 2017. DOI: 10.1109/MDAT.2016.2573586

- [2] M. Suri, O. Bichler, D. Querlioz, O. Cueto, L. Perniola, V. Sousa, D. Vuillaume, C. Gamrat, and B. DeSalvo, "Phase change memory as synapse for ultra-dense neuromorphic systems: Application to complex visual pattern extraction", in 2011 International Electron Devices Meeting, pp. 4.4.1-4.4.4, Dec. 2011. DOI: 10.1109/IEDM.2011.6131488
- [3] G. W. Burr, R. M. Shelby, S. Sidler, C. di Nolfo, J. Jang, I. Boybat, R. S. Shenoy, P. Narayanan, K. Virwani, E. U. Giacometti, B. N. Kurdi, and H. Hwang, "Experimental Demonstration and Tolerancing of a Large-Scale Neural Network (165 000 Synapses) Using Phase-Change Memory as the Synaptic Weight Element", IEEE Trans. Electron Devices, vol. 62, no. 11, pp. 3498 3507, Nov. 2015. DOI: 10.1109/TED.2015.2439635
- [4] I. Boybat, M. L. Gallo, S. R. Nandakumar, T. Moraitis, T. Parnell, T. Tuma, B. Rajendran, Y. Leblebici, A. Sebastian, and E. Eleftheriou, "Neuromorphic computing with multi-memristive synapse", Nature Communications, vol. 9, pp. 1-12, Jun. 2018, Art. no. 2514. DOI: 10.1038/s41467-018-04933-y
- [5] S. Yu, Y. Wu, R. Jeyasingh, D. Kuzum, and H.-S. P. Wong, "An Electronic Synapse Device Based on Metal Oxide Resistive Switching Memory for Neuromorphic Computation", IEEE Trans. Electron Devices, vol. 58, no.8, pp. 2729 2737, Aug. 2011. DOI: 10.1109/TED.2011.2147791
- [6] P. Yao, H. Wu, B. Gao, S. B. Eryilmaz, X. Huang, W. Zhang, Q. Zhang, N. Deng, L. Shi, H.-S. P. Wong, and H. Qian, "Face classification using electronic synapses", Nature Communications, vol. 8, pp. 1-8, May 2017, Art. no. 15199. DOI: 10.1038/ncomms15199
- [7] A. F. Vincent, J. Larroque, N. Locatelli, N. B. Romdhane, O. Bichler, C. Gamrat, W. S. Zhao, J.-O. Klein, S. G.-Retailleau, and D. Querlioz, "Spin-Transfer Torque Magnetic Memory as a Stochastic Memristive Synapse for Neuromorphic Systems", IEEE Transactions on Biomedical Circuits and Systems, vol.9, no. 2, pp. 166 174, Apr. 2015. DOI: 10.1109/TBCAS.2015.2414423
- [8] S. Ambrogio, P. Narayanan, H. Tsai, R. M. Shelby, I. Boybat, C. di Nolfo, S. Sidler, M. Giordano, M. Bodini, N. C. P. Farinha, B. Killeen, C. Cheng, Y. Jaoudi, and G. W. Burr, "Equivalent-accuracy accelerated neural-network training using analogue memory", Nature, vol. 558, pp. 60–67, Jun. 2018. DOI: https://doi.org/10.1038/s41586-018-0180-5
- [9] D. Kaushik, U. Singh, U. Sahu, I. Sreedevi, and D. Bhowmik, "Comparing domain wall synapse with other non volatile memory devices for on chip learning in analog hardware neural network", AIP Advances, vol. 10, no. 2, pp. 1-7, Feb. 2020, Art. no. 025111. DOI: https://doi.org/10.1063/1.5128344
- [10] M. A. Azam, D. Bhattacharya, D. Querlioz, C.A. Ross, and J. Atulasimha, "Voltage control of domain walls in magnetic nanowires for energy-efficient neuromorphic devices", Nanotechnology, vol. 31, no. 14, pp. 1-9, Jan. 2020, Art. no. 145201. DOI: https://doi.org/10.1088/1361-6528/ab6234
- [11] S. Lequeux, J. Sampaio, V. Cros, K. Yakushiji, A. Fukushima, R. Matsumoto, H. Kubota, S. Yuasa, and J. Grollier, "A magnetic synapse: multilevel spin-torque memristor with perpendicular anisotropy", Scientific Reports, vol. 6, pp. 1-7, Aug. 2016, Art. no. 31510. DOI: 10.1038/srep31510
- [12] D. M. F. Hartmann, R. A. Duine, M. J. Meijer, H. J.M. Swagten, and R. Lavrijsen, "Creep of chiral domain walls", Phys. Rev. B, vol. 100, no. 1, pp. 1-5, Sep. 2019, Art. no. 094417. DOI: 10.1103/PhysRevB.100.094417

- [13] E. Martinez, S. Emori, and G. S. D. Beach, "Current-driven domain wall motion along high perpendicular anisotropy multilayers: The role of the Rashba field, the spin Hall effect, and the Dzyaloshinskii-Moriya interaction", Appl. Phys. Lett., vol. 103, no. 7, pp. 1-5, Jul. 2013, Art. no. 072406. DOI: https://doi.org/10.1063/1.4818723
- [14] A. V. Khvalkovskiy, V. Cros, D. Apalkov, V. Nikitin, M. Krounbi, K. A. Zvezdin, A. Anane, J. Grollier, and A. Fert, "Matching domain-wall configuration and spinorbit torques for efficient domain-wall motion", Phys. Rev. B, vol. 87, no. 2, pp. 1-5, Jan. 2013, Art. no. 020402(R).DOI:https://doi.org/10.1103/PhysRevB.87.0 20402
- [15] D. Bhowmik, M. E. Nowakowski, L. You, O. Lee, D. Keating, M. Wong, J. Bokor, and S. Salahuddin, "Deterministic Domain Wall Motion Orthogonal To Current Flow Due To Spin Orbit Torque", vol. 5, pp. 1-10, Jul. 2015, Art. no. 11823. DOI: 10.1038/srep11823
- [16] A. Thiaville, Y. Nakatani, J. Miltat, and N. Vernier, "Domain wall motion by spin-polarized current: a micromagnetic study", Journal of Applied Physics, vol. 95, no. 11, pp. 7049-7051, May 2004. DOI: https://doi.org/10.1063/1.1667804
- [17] P. Chureemart, R. F. L. Evans, and R. W. Chantrell, "Dynamics of domain wall driven by spin-transfer torque", Phys. Rev. B, vol. 83, no. 18, pp. 1-8, May 2011, Art. no. 184416. DOI: 10.1088/0953-8984/24/2/024221
- [18] B. Zhang, Y. Xu, W. Zhao, D. Zhu, H. Yang, X. Lin, M. Hehn, G. Malinowski, N. Vernier, D. Ravelosona, and S. Mangin, "Domain-wall motion induced by spin transfer torque delivered by helicity-dependent femtosecond laser", Phys. Rev. B, vol. 99, no. 14, pp. 1-6, Apr. 2019, Art. no. 144402. DOI: https://doi.org/10.1103/PhysRevB.99.144402
- [19] N. Lei, T. Devolder, G. Agnus, P. Aubert, L. Daniel, J.-V. Kim, W. Zhao, T. Trypiniotis, R. P. Cowburn, C. Chappert, D. Ravelosona, and P. Lecoeur, "Straincontrolled magnetic domain wall propagation in hybrid piezoelectric/ferromagnetic structures", Nature Communications, vol. 4, pp. 1-7, Jan 2013, Art. no. 1378 DOI: 10.1038/ncomms2386.
- [20] H. T. Chena and A. K. Soh, "Precision electric control of magnetic domain wall motions in a multiferroic bilayer based on strain-mediated magnetoelectric coupling", Materials Research Bulletin, vol. 59, pp. 42-48, Nov. 2014. DOI: https://doi.org/10.1016/j.materresbull.2014.06.023
- [21] Q. Wang, J. Z. Hu, C.Y. Liang, A. Sepulveda, and G. Carman, "Voltage-induced strain clocking of nanomagnets with perpendicular magnetic anisotropies", Sci. Rep., vol. 9, pp. 1-7, Mar. 2019, Art. no. 3639. DOI: https://doi.org/10.1038/s41598-019-39966-w
- [22] S. Giordano, Y. Dusch, N. Tiercelin, P. Pernod, and V. Preobrazhensky, "Combined nanomechanical and nanomagnetic analysis of magnetoelectric memories", Physical Review B, vol. 85, no. 15, pp. 1-14, Apr. 2012, Art. no. 155321. DOI: https://doi.org/10.1103/PhysRevB.85.155321
- [23] K. Roy, S. Bandyopadhyay, and J. Atulasimha, "Hybrid spintronics and straintronics: A magnetic technology for ultra low energy computing and signal processing", Appl. Phys. Lett., vol. 99, no. 6, pp. 1-3, Jul. 2011, Art. no. 063108. DOI: https://doi.org/10.1063/1.3624900
- [24] J. Atulasimha and S. Bandyopadhyay, "Bennett clocking of nanomagnetic logic using multiferroic single-domain nanomagnets", Appl. Phys. Lett., vol. 97, no. 17, pp. 1-3, Oct. 2010, Art. no. 173105. DOI: https://doi.org/10.1063/1.3506690

- [25] K. Roy, S. Bandyopadhyay, and J. Atulasimha, "Binary switching in a 'symmetric' potential landscape", Sci. Rep., vol. 3, pp. 1-8, Oct. 2013, Art. no. 3038. DOI: 10.1038/srep03038
- [26] N. D'Souza, M. S. Fashami, S. Bandyopadhyay, and J. Atulasimha, "Experimental Clocking of Nanomagnets with Strain for Ultralow Power Boolean Logic", Nano Lett., vol. 16, no. 2, pp. 1-8, Jan. 2016. DOI: https://doi.org/10.1021/acs.nanolett.5b04205
- [27] A. K Biswas, H. Ahmad, J. Atulasimha, and S. Bandyopadhyay, "Experimental Demonstration of Complete 180° Reversal of Magnetization in Isolated Co Nanomagnets on a PMN-PT Substrate with Voltage Generated Strain", Nano Lett. vol. 17, no. 6, pp. 3478–3484, May. 2017. DOI: https://doi.org/10.1021/acs.nanolett.7b00439
- [28] A. W. Rushforth, R. R. Robinson, and J Zemen, "Deterministic magnetic domain wall motion induced by pulsed anisotropy energy", J. Phys. D: Appl. Phys., vol. 53, no. 16, pp. 1-7, Feb. 2020, Art. no. 164001. DOI: https://doi.org/10.1088/1361-6463/ab6cc7
- [29] T. Mathurin, S. Giordano, Y. Dusch, N. Tiercelin, P. Pernod, and V. Preobrazhensky, "Stress-mediated magnetoelectric control of ferromagnetic domain wall position in multiferroic heterostructures", Appl. Phys. Lett., vol. 108, no. 8, pp. 1-5, Feb. 2016, Art. no. 082401. DOI: https://doi.org/10.1063/1.4942388
- [30] V. Uhlíř, S. Pizzini, N. Rougemaille, J. Novotný, V. Cros, E. Jiménez, G. Faini, L. Heyne, F. Sirotti, C. Tieg, A. Bendounan, F. Maccherozzi, R. Belkhou, J. Grollier, A. Anane, and J. Vogel, "Current-induced motion and pinning of domain walls in spin-valve nanowires studied by XMCD-PEEM", Phys. Rev. B, vol. 81, no. 22, pp. 1-10, Jun. 2010, Art. no. 224418. DOI: https://doi.org/10.1103/PhysRevB.81.224418
- [31] X. Jiang, L. Thomas, R. Moriya, M. Hayashi, B. Bergman, C. Rettner, and S. S.P. Parkin, "Enhanced stochasticity of domain wall motion in magnetic racetracks due to dynamic pinning", Nature Communications, vol. 1, pp. 1-5, Jun. 2010, Art. no: 25. DOI: 10.1038/ncomms1024
- [32] J. P. Attan´e, D. Ravelosona, A. Marty, Y. Samson, and C. Chappert, "Thermally Activated Depinning of a Narrow Domain Wall from a Single Defect", Phys. Rev. Lett., vol. 96, no. 14, pp. 1-4, Apr. 2006, Art. no. 147204. DOI: https://doi.org/10.1103/PhysRevLett.96.147204.
- [33] R. Lewis, D. Petit, L. Thevenard, A. V. Jausovec, L. O'Brien, D. E. Read, and R. P. Cowburn, "Magnetic domain wall pinning by a curved conduit", Appl. Phys. Lett., vol. 95, no. 15, pp. 1-3, Oct. 2009, Art. no. 152505. DOI: https://doi.org/10.1063/1.3246154
- [34] D. Petit, A.-V. Jausovec, D. Read, and R. P. Cowburn, "Domain wall pinning and potential landscapes created by constrictions and protrusions in ferromagnetic nanowires", J. Appl. Phys., vol. 103, no. 11, pp. 1-6, Jun. 2008, Art. no. 114307. DOI: https://doi.org/10.1063/1.2936981
- [35] M. Albert, M. Franchin, T. Fischbacher, G. Meier, and H. Fangohr, "Domain wall motion in perpendicular anisotropy nanowires with edge roughness", Journal of Physics: Condensed Matter, vol. 24, no. 2, pp. 1-14, Dec. 2011, Art. no. 024219. DOI: 10.1088/0953-8984/24/2/024219
- [36] S. Dutta, S. A. Siddiqui, J. A. Currivan-Incorvia, C. A. Ross, and M. A. Baldo, "The Spatial Resolution Limit for an Individual Domain Wall in Magnetic Nanowires", Nano Lett., vol. 17, no. 9, pp. 5869–5874, Aug. 2017. DOI: https://doi.org/10.1021/acs.nanolett.7b03199
- [37] I. Hubara, M. Courbariaux, D. Soudry, R. El-Yaniv, and Y. Bengio, "Quantized Neural Networks: Training

- Neural Networks with Low Precision Weights and Activations", The Journal of Machine Learning Research vol. 18, no. 187, pp. 1-30, Apr. 2017.
- [38] B. Jacob, S. Kligys, B. Chen, M. Zhu, M. Tang, A. Howard, H. Adam, and D. Kalenichenko, "Quantization and Training of Neural Networks for Efficient Integer-Arithmetic-Only Inference", arXiv:1712.05877, Dec. 2017
- [39] F. Li, B. Zhang, and B. Liu, "Ternary weight networks", arXiv:1605.04711, May 2016.
- [40] V. Joshi, M. Le Gallo, S. Haefeli, I. Boybat, S. R. Nandakumar, C. Piveteau, M. Dazzi, B. Rajendran, A. Sebastian, and E. Eleftheriou, "Accurate deep neural network inference using computational phase-change memory", Nature Communications, vol. 11, pp. 1-13, May 2020, Art. no: 2473. DOI: https://doi.org/10.1038/s41467-020-16108-9
- [41] S. Emori, U. Bauer, S.-M. Ahn, E. Martinez, and G. S. D. Beach, "Current-driven dynamics of chiral ferromagnetic domain walls", Nat. Mater., vol. 12, pp. 611–616, Jun. 2013. DOI:10.1038/NMAT3675
- [42] J. A. Currivan, S. Siddiqui, S. Ahn, L. Tryputen, G. S. D. Beach, Marc A. Baldo, Caroline A. Ross, "Polymethyl methacrylate/hydrogen silsesquioxane bilayer resist electron beam lithography process for etching 25 nm wide magnetic wires", J. Vac. Sci. Technol. B, vol. 32, no. 2, pp. 1-5, Feb. 2014, Art. no. 021601. doi: https://doi.org/10.1116/1.4867753
- [43] A. Vansteenkiste, J. Leliaert, M. Dvornik, M. Helsen, F. Garcia-Sanchez, and B. V. Waeyenberge, "The design and verification of MuMax3", AIP Advances, vol. 4, no. 10, pp. 1-22, Oct. 2014, Art. no. 107133. DOI: https://doi.org/10.1063/1.4899186
- [44] L. Liu, R. A. Buhrman, and D. C. Ralph, "Review and Analysis of Measurements of the Spin Hall Effect in Platinum", arXiv:1111.3702, Mar. 2012.
- [45] C. J. G.-Cervera, Z. Gimbutas, and Weinan E, "Accurate numerical methods for micromagnetics simulations with general geometries", Journal of Computational Physics, vol. 184, no. 1, pp. 37-52, Jan. 2003. DOI: https://doi.org/10.1016/S0021-9991(02)00014-1
- [46] G. J. Parker, C. Cerjan, and D. W. Hewett, "Embedded curve boundary method for micromagnetic simulations", Journal of Magnetism and Magnetic Materials, vol. 214, no. 1-2, pp. 130-138, May. 2000. DOI: https://doi.org/10.1016/S0304-8853(00)00043-3
- [47] M. J. Donahue, and R. D. McMichael, "Micromagnetics on Curved Geometries Using Rectangular Cells: Error Correction and Analysis", IEEE Transactions on Magnetics, vol. 43, no. 6, pp. 2878 - 2880, Jun. 2007. DOI: 10.1109/TMAG.2007.892865
- [48] J. Cui, J. L. Hockel, P. K. Nordeen, D. M. Pisani, C.-Y. Liang, G. P. Carman, and C. S. Lynch, "A method to control magnetism in individual strain-mediated magnetoelectric islands", Appl. Phys. Lett., vol. 103, no. 23, pp. 1-5, Dec. 2013, Art. no. 232905. DOI: https://doi.org/10.1063/1.4838216
- [49] G. Bertotti, I. D. Mayergoyz, and C. Serpico, "Stochastic magnetization dynamics," in *Nonlinear Magnetization Dynamics in Nanosystems*, Amsterdam, The Netherlands: Elsevier, 2009, ch 10, pp-271-345.
- [50] C. Bilzera, T. Devolder, J.-V. Kim, G. Counil, and C. Chappert, "Study of the dynamic magnetic properties of soft CoFeB films", J. Appl. Phys., vol. 100, no. 5, pp. 1-4, Sep. 2006, Art. no. 053903. DOI: https://doi.org/10.1063/1.2337165
- [51] M. Belmeguenai, M. S. Gabor, Y. Roussign'e, A. Stashkevich, S. M. Ch'erif, F. Zighem, and C. Tiusan, "Brillouin light scattering investigation of the thickness dependence of Dzyaloshinskii-Moriya interaction in

- Co0.5Fe0.5 ultrathin films", Physical Review B, vol. 93, no. 17, pp. 1-8, May 2016, Art. no. 174407. DOI: https://doi.org/10.1103/PhysRevB.93.174407
- [52] D. Hunter, W. Osborn, K. Wang, N. Kazantseva, J. H.-Simpers, R. Suchoski, R. Takahashi, M. L. Young, A. Mehta, L. A. Bendersky, S. E. Lofland, M. Wuttig, and I. Takeuchi, "Giant magnetostriction in annealed Co1-x Fex thin-films", Nature Communications, vol. 2, pp. 1-7, Nov. 2011, Art. no: 518. DOI: 10.1038/ncomms1529
- [53] S. Dutta, S. A. Siddiqui, J. A. Currivan-Incorvia, C. A. Ross, and M. A. Baldo, Micromagnetic modeling of domain wall motion in sub-100-nm-wide wires with individual and periodic edge defects, AIP Advances 5, 127206 (2015), doi:https://doi.org/10.1063/1.4937557
- [54] T. Suzukia, S. Fukami, N. Ohshima, K. Nagahara, and N. Ishiwata, Analysis of current-driven domain wall motion from pinning sites in nanostrips with perpendicular magnetic anisotropy, Journal of Applied Physics 103, 113913 (2008), doi:https://doi.org/10.1063/1.2938843
- [55] Takashi Komine, Hiroshi Murakami, Takahiro Nagayama, Ryuji Sugita, Influence of Notch Shape and Size on Current-Driven Domain Wall Motions in a Magnetic Nanowire, IEEE Transactions on Magnetics, Vol. 44, no.11, pp. 2516 - 2518, Nov. 2008, DOI: 10.1109/TMAG.2008.2002614
- [56] J. Torrejon, E. Martinez, and M. Hayashi, "Tunable inertia of chiral magnetic domain walls", Nature Communications, vol. 7, pp. 1-7, Nov. 2016, Art. no: 13533. DOI: 10.1038/ncomms13533
- [57] A. Thiaville, S. Rohart, É. Jué, V. Cros, and A. Fert, "Dynamics of Dzyaloshinskii domain walls in ultrathin magnetic films", EPL (Europhysics Letters), vol. 100, no. 5, pp. 1-6, Dec. 2012, Art. no. 57002. DOI: 10.1209/0295-5075/100/57002
- [58] A. Mohanty, X. Du, P.-Yu Chen, J. Seo, S. Yu, Y. Cao, "Random sparse adaptation for accurate inference with inaccurate multi-level RRAM arrays", in 2017 IEEE International Electron Devices Meeting (IEDM), Dec. 2017, DOI: 10.1109/IEDM.2017.8268339
- [59] M. Hu, H. Li, Y. Chen, Q. Wu, G. S. Rose. "BSB training scheme implementation on memristor-based circuit", in 2013 IEEE Symposium on Computational Intelligence for Security and Defense Applications (CISDA), Apr. 2013. DOI: 10.1109/CISDA.2013.6595431
- [60] B. Liu, H. Li, Y. Chen, X. Li, T. Huang, Q. Wu, and M. Barnell, "Reduction and IR-drop compensations techniques for reliable neuromorphic computing systems", in 2014 IEEE/ACM International Conference on Computer-Aided Design (ICCAD), Jan. 2015. DOI: 10.1109/ICCAD.2014.7001330
- [61] T. Hirtzlin, M. Bocquet, B. Penkovsky, J.-O. Klein, E. Nowak, E. Vianello, J.-M. Portal, and D. Querlioz, "Digital Biologically Plausible Implementation of Binarized Neural Networks With Differential Hafnium Oxide Resistive Memory Arrays", Frontiers in Neuroscience, Vol. 13, pp.1-14, Jan. 2020, Art. no. 1383, doi: https://doi.org/10.3389/fnins.2019.01383
- [62] H.-S. Philip Wong, and S. Salahuddin, Memory leads the way to better computing, Nature Nanotechnology, vol 10, pp. 191-194, Mar. 2015.doi: https://doi.org/10.1038/nnano.2015.29